MITSUBISHI ELECTRIC RESEARCH LABORATORIES
https://www.merl.com

# Sensorless Control of Synchronous Machines with DC-Link Voltage Immunity and Adaptation

Anantaram, Varatharajan; Wang, Yebin

TR2022-165 December 16, 2022

**Abstract**

Position sensorless techniques have implicit dependence on the DC-link voltage sensor which acts as a single point of failure. This work presents a novel position estimation technique that is immune and resilient to the errors in the DC-link voltage measurement. The proposed sensorless scheme is developed within the projection vector framework from the linearized dynamics of the hybrid flux observer. In addition, a DC-link voltage estimation that is independent and decoupled from the position estimation is developed for a potential DC-link voltage sensorless and position sensorless operation capability. The proposed scheme is validated in simulations on a 5.5 kW permanent magnet assisted synchronous reluctance (PM-SyR) machine.

*IEEE Power Electronics, Drives and Energy Systems 2022*



Mitsubishi Electric Research Laboratories, Inc.
201 Broadway, Cambridge, Massachusetts 02139

# Sensorless Control of Synchronous Machines with DC-Link Voltage Immunity and Adaptation

Anantaram Varatharajan
*Mitsubishi Electric Research Laboratories*
Cambridge, Massachusetts 02139, USA
varatharajan@ieee.org

Yebin Wang
*Mitsubishi Electric Research Laboratories*
Cambridge, Massachusetts 02139, USA
yebinwang@ieee.org

***Abstract*—Position sensorless techniques have implicit dependence on the DC-link voltage sensor which acts as a single point of failure. This work presents a novel position estimation technique that is immune and resilient to the errors in the DC-link voltage measurement. The proposed sensorless scheme is developed within the projection vector framework from the linearized dynamics of the hybrid flux observer. In addition, a DC-link voltage estimation that is independent and decoupled from the position estimation is developed for a potential DC-link voltage sensorless and position sensorless operation capability. The proposed scheme is validated in simulations on a 5.5 kW permanent magnet assisted synchronous reluctance (PM-SyR) machine.**

***Index Terms*—Sensorless control, DC-link voltage immunity, projection vector, synchronous machines.**

## I. Introduction

An accurate and reliable DC-link voltage measurement is essential for normal operation of motor drives and, in particular, for position estimation in sensorless motor drives. The fluctuations in the DC-link voltage may occur due to multiple reasons: *(i)* the DC-link capacitors are voluminous in size and down-sizing may be desirable for compactness of the motor drive system which, for systems with diode-bridge passive front end, leads to reduction in stiffness and oscillation in the DC-link voltage at high load; *(ii)* a weak grid is susceptible to voltage dips and surges if faults occur in the vicinity; *(iii)* the battery powered servo-drive and propulsion applications see DC-link voltage variations as a function of the battery state-of-charge.

Typically, the DC-link voltage is measured and the PWM duty cycles are generated to realize the reference voltage; this minimizes the impact of the DC-link voltage fluctuations, provided the operating point is below the voltage limit. The voltage sensor could be subjected to temperature inflation, electromagnetic interference and other external factors in harsh working environments. In the absence of a reliable bus voltage measurement, the discrepancy between the reference voltage and output inverter voltage manifests as torque error and ripples in the motor, adversely impacting the load [1], [2]. The sensorless control techniques without a position transducer can be broadly classified into two categories: *(i)* high-frequency excitation schemes for zero to low speeds region [3], [4]; *(ii)* fundamental excitation schemes for medium to high speeds region [5], [6]. The latter schemes are strongly coupled to the fundamental voltage and flux quantities, making it more sensitive to the DC-link voltage. The malfunctioning of the voltage sensor hampers the sensorless operation that risks instability, and poses a threat of single point of failure.

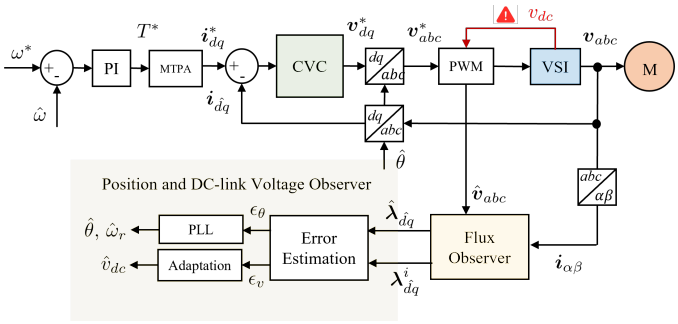


Fig. 1. Block diagram of the proposed sensorless control scheme using current vector control (CVC) with hybrid flux observer and DC-link voltage adaptation.

The faults in the DC-link voltage sensor are detected from the balancing the estimated electrical input power and the output mechanical power in [7], and if it exceeds a certain threshold, the the nominal DC-link voltage is used. An adaptive observer is used to estimate the DC-link voltage and the rotor resistance of an induction machine in [8]. A sliding mode observer is used for DC-link voltage estimation in [9], [10]. However, all of the cited works rely on the measured position for DC-link voltage estimation. To the author's knowledge, the impact of faults in the DC-link voltage sensor on sensorless motor drives has not been dealt before in the literature.

This work presents a novel sensorless control technique for permanent magnet assisted synchronous reluctance (PM-SyR) motor that is independent and immune to the errors in DC-link voltage measurement; the block diagram of the proposeed scheme is shown in Fig. 1. This can be repurposed as a tool for diagnosis/post-fault operation should the voltage sensor fail in critical applications. The main contributions of this work are:

1) A projection vector based position observer is designed from the linearized error dynamics of the hybrid flux observer such that it is independent of the DC-link voltage error in steady-state.
2) Unlike the state-of-art sensorless techniques where an error in the bus voltage measurement causes a steady-state

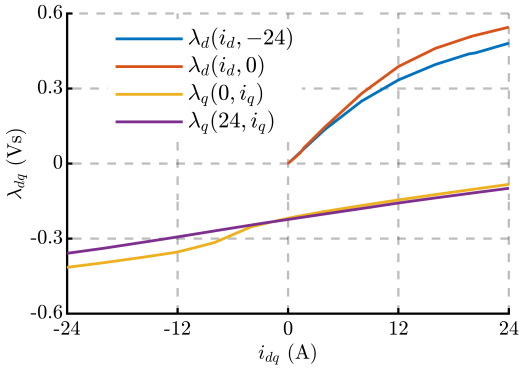


Fig. 2. Flux map of the 5.5 kW PM-SyR motor under test exhibiting saturation and cross-saturation characteristics. Experimentally identified with the constant speed test, reported in [11].

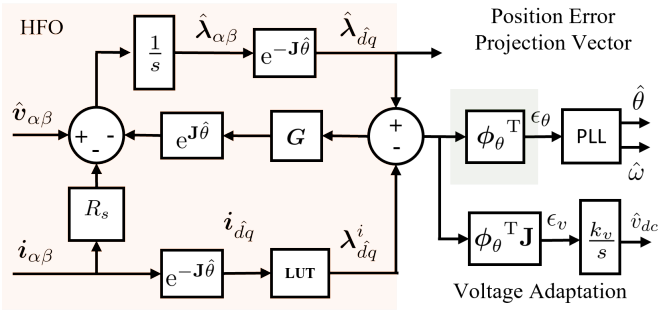


Fig. 3. Projection vector-based sensorless control technique for DC-link voltage error immunity. Shown are the hybrid flux observer and the proposed scheme exploiting two degrees of freedom for position estimation and parameter adaptation.

position error if not instability, the proposed scheme is immune and stable.

3) In order to improve the torque and flux estimation accuracy, a supplementary DC-link voltage adaptation is designed exploiting the two degrees of freedom.

Section II introduces the sensorless control system and Section III presents the proposed scheme using projection vector framework. Section IV discusses the simulation results and Section V concludes the paper.

## II. Sensorless Control System

The electrical rotor position is $\theta$ and the electrical angular speed is $\omega = s\,\theta$ where $s$ is the differential operator $\frac{\mathrm{d}}{\mathrm{d}t}$. Estimated vectors are represented by the superscript $\hat{}$. The orthogonal rotational matrix is $\mathbf{J} = \left[\begin{smallmatrix} 0 & -1 \\ 1 & 0 \end{smallmatrix}\right]$ and $\mathbf{I}$ is the identity matrix.

The machine model is expressed in coordinates of estimated rotor reference frame, denoted by subscript $\hat{d}q$, whose $\hat{d}$-axis is at $\hat{\theta} = \theta - \tilde{\theta}$, where $\tilde{\theta}$ is the position error. Real space vectors will be used; for example, the stator current is $\boldsymbol{i}_{\hat{d}q} = [i_{\hat{d}}, i_{\hat{q}}]^{\mathrm{T}}$ where $i_{\hat{d}}$ and $i_{\hat{q}}$ are the vector components in the estimated rotor reference frame. Space vectors in the stationary reference frame are denoted by subscript $\alpha\beta$. Note that the convention of a synchronous reluctance (SyR) machine is followed, i.e, $d$-axis is defined along the maximum inductance path.

### A. Mathematical Model of a Synchronous Machine

The voltage equation of a synchronous machine in the estimated rotor reference frame is given by

$$s\,\boldsymbol{\lambda}_{\hat{d}q} = \boldsymbol{v}_{\hat{d}q} - R_s \boldsymbol{i}_{\hat{d}q} - \hat{\omega}\,\mathbf{J}\,\boldsymbol{\lambda}_{\hat{d}q} \tag{1}$$

where $R_s$ is the stator resistance and $\boldsymbol{\lambda}_{\hat{d}q}$ is the stator flux linkage. The synchronous machine exhibits nonlinear magnetic characteristics due to both saturation and cross-saturation phenomenon. Equivalently, the nonlinear stator flux linkage can be expressed as an operating point dependent linear magnetic model as

$$\boldsymbol{\lambda}_{\hat{d}q} = \mathrm{e}^{\mathbf{J}\tilde{\theta}}\,\boldsymbol{L}(\boldsymbol{i}_{dq})\,\mathrm{e}^{-\mathbf{J}\tilde{\theta}}\,\boldsymbol{i}_{\hat{d}q} + \mathrm{e}^{\mathbf{J}\tilde{\theta}}\,\boldsymbol{\lambda}_m \tag{2}$$

where the apparent inductance matrix $\boldsymbol{L}$ is a function of the operating point $\boldsymbol{i}_{dq}$ in the real $dq$ rotor reference frame and $\boldsymbol{\lambda_m}$ is the open circuit permanent-magnet flux vector. They are given by

$$\boldsymbol{L}(\boldsymbol{i}_{dq}) = \begin{bmatrix} L_d & 0 \\ 0 & L_q \end{bmatrix} \quad \boldsymbol{\lambda}_m = \begin{bmatrix} 0 \\ -\lambda_m \end{bmatrix} \tag{3}$$

where $\lambda_m$ is the open circuit permanent-magnet flux linkage and $L_d, L_q$ are the apparent inductances along $d$ and $q$-axis, respectively. The average electromagnetic torque is given by

$$T = \frac{3p}{2}\,\boldsymbol{i}_{\hat{d}q}^{\mathrm{T}}\,\mathbf{J}\,\boldsymbol{\lambda}_{\hat{d}q} \tag{4}$$

where $p$ is the number of pole pairs.

### B. Hybrid Flux Observer

*1) State Equation:* The hybrid flux observer is a combination of the back-emf integral (voltage-model) and the current-model fluxes, defined in the stationary reference frame as

$$s\hat{\boldsymbol{\lambda}}_{\alpha\beta} = \hat{\boldsymbol{v}}_{\alpha\beta} - R_s \boldsymbol{i}_{\alpha\beta} + \mathrm{e}^{\mathbf{J}\hat{\theta}}\,\boldsymbol{G}\left(\boldsymbol{\lambda}^{i}_{\hat{d}q} - \hat{\boldsymbol{\lambda}}_{\hat{d}q}\right) \tag{5}$$

where $\boldsymbol{G}$ is a $2\times 2$ gain matrix and $\boldsymbol{\lambda}^{i}_{\hat{d}q}$ is current-model flux linkage based on the flux-map LUTs; Accurate parameters are assumed in this work, i.e., $\boldsymbol{\lambda}^{i}_{dq} = \boldsymbol{\lambda}_{dq}$. For analysis purposes, the state equation is transformed to synchronous reference frame as

$$s\,\hat{\boldsymbol{\lambda}}_{\hat{d}q} = \hat{\boldsymbol{v}}_{\hat{d}q} - R_s \boldsymbol{i}_{\hat{d}q} - \hat{\omega}\mathbf{J}\,\hat{\boldsymbol{\lambda}}_{\hat{d}q} + \boldsymbol{G}\left(\boldsymbol{\lambda}^{i}_{\hat{d}q} - \hat{\boldsymbol{\lambda}}_{\hat{d}q}\right) \tag{6}$$

where $\tilde{\boldsymbol{v}}_{\hat{d}q} = \boldsymbol{v}_{\hat{d}q} - \hat{\boldsymbol{v}}_{\hat{d}q}$ is the voltage error. The error in the DC-link voltage appears as a scalar gain on the fundamental voltage and is related to the voltage error as

$$\tilde{\boldsymbol{v}}_{\hat{d}q} = \boldsymbol{v}_{\hat{d}q}\,\tilde{v}_{dc} \tag{7}$$

where $\tilde{v}_{dc} = (v_{dc} - \hat{v}_{dc})/v_{dc,n}$ is the relative error and $v_{dc,n}$ is the nominal voltage.

*2) Small-Signal Model:* The relationship between the real stator flux $\boldsymbol{\lambda}_{\hat{d}q}$ and the current model estimate $\boldsymbol{\lambda}^{i}_{\hat{d}q}$ in the estimated reference frame is formulated by linearizing the stator flux linkage around an operating point as

$$\begin{aligned}\boldsymbol{\lambda}_{\hat{d}q}(\boldsymbol{i}_{dq}) &= \mathrm{e}^{\mathbf{J}\tilde{\theta}}\,\boldsymbol{\lambda}_{dq}(\mathrm{e}^{-\mathbf{J}\tilde{\theta}}\boldsymbol{i}_{\hat{d}q}) \\ &\approx \left(\mathbf{I}+\tilde{\theta}\,\mathbf{J}\right)\left(\boldsymbol{\lambda}_{dq}(\boldsymbol{i}_{\hat{d}q}) - \tilde{\theta}\,\frac{\partial\boldsymbol{\lambda}_{dq}}{\partial\boldsymbol{i}_{\hat{d}q}}\,\mathbf{J}\,\boldsymbol{i}_{\hat{d}q}\right) \end{aligned} \tag{8}$$

The time derivative of stator flux can be expressed with the incremental inductance matrix $\boldsymbol{L}_{\partial}$ as

$$\frac{\partial\boldsymbol{\lambda}_{dq}}{\partial\boldsymbol{i}_{dq}} = \boldsymbol{L}_{\partial}(\boldsymbol{i}_{dq}) = \begin{bmatrix} l_d & l_{dq} \\ l_{dq} & l_q \end{bmatrix} \tag{9}$$

where $l_d, l_q$ represents the $d$ and $q$-axis incremental inductance, respectively, and $l_{dq}$ is the cross-saturation term. The first order approximation holds for small position error, i.e., a constant incremental inductance in the vicinity of the operating point is assumed. Simplifying (8), the magnetic model accounting position error (MMAP) is derived as

$$\boldsymbol{\lambda}_{\hat{d}q} = \boldsymbol{\lambda}^{i}_{\hat{d}q} + \tilde{\theta}\,\boldsymbol{\lambda}^{a}_{\hat{d}q} \tag{10}$$

where the auxiliary-flux vector $\boldsymbol{\lambda}^{a}_{\hat{d}q}$ for nonlinear magnetic model is given by

$$\boldsymbol{\lambda}^{a}_{\hat{d}q} = \mathbf{J}\,\boldsymbol{\lambda}^{i}_{\hat{d}q} - \boldsymbol{L}_{\partial}\,\mathbf{J}\,\boldsymbol{i}_{\hat{d}q}. \tag{11}$$

To aid in further analysis, the nonlinear flux estimation error dynamics is derived from (1) and (6) as

$$s\,\tilde{\boldsymbol{\lambda}}_{\hat{d}q} = \tilde{\boldsymbol{v}}_{\hat{d}q} - (\boldsymbol{G}+\hat{\omega}\mathbf{J})\,\tilde{\boldsymbol{\lambda}}_{\hat{d}q} + \boldsymbol{G}\,(\boldsymbol{\lambda}_{\hat{d}q} - \boldsymbol{\lambda}^{i}_{\hat{d}q}) \tag{12}$$

where $\tilde{\boldsymbol{\lambda}}_{\hat{d}q} = \boldsymbol{\lambda}_{\hat{d}q} - \hat{\boldsymbol{\lambda}}_{\hat{d}q}$ is the flux estimation error. Using MMAP (10) in (12), the linearized flux estimation error dynamics as a function of position error is given by

$$\tilde{\boldsymbol{\lambda}}_{\hat{d}q} = (s\mathbf{I}+\boldsymbol{G}+\omega\mathbf{J})^{-1}\,(\tilde{\boldsymbol{v}}_{\hat{d}q} + \boldsymbol{G}\,\boldsymbol{\lambda}^{a}_{\hat{d}q}\,\tilde{\theta}). \tag{13}$$

This will be used in the following section to formulate the position error signal.

## III. Projection Vector Framework

### A. Definition

The generalized error signal $\epsilon$ driving the observer adaptation law is expressed as the projection of difference in the observed and the current-model flux estimates on a projection vector $\boldsymbol{\phi}$ [12] [5] as

$$\epsilon = \boldsymbol{\phi}^{\mathrm{T}}\,(\hat{\boldsymbol{\lambda}}_{\hat{d}q} - \boldsymbol{\lambda}^{i}_{\hat{d}q}). \tag{14}$$

The linearized form the error signal is derived using (10) as

$$\epsilon = \boldsymbol{\phi}^{\mathrm{T}}\,\big(\hat{\boldsymbol{\lambda}}^{a}_{\hat{d}q}\,\tilde{\theta} - \tilde{\boldsymbol{\lambda}}_{\hat{d}q}\big). \tag{15}$$

This will be used for the position tracking and the DC-link voltage estimation. Following the results of the flux estimation error dynamics (13), the error signal (15) is decomposed in terms of the constituent errors as

$$\epsilon = \boldsymbol{\phi}^{\mathrm{T}}\,\begin{bmatrix}\boldsymbol{h}_{\theta} & \boldsymbol{h}_{v}\end{bmatrix}\,\tilde{\boldsymbol{x}} \tag{16a}$$

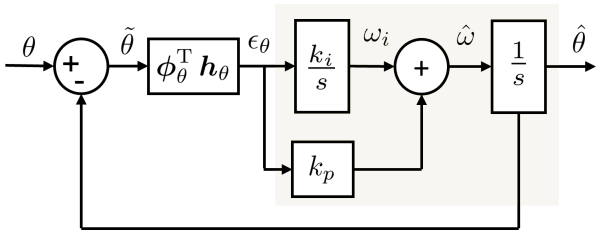


Fig. 4. Block diagram of the closed loop transfer function of the position estimation loop (22).

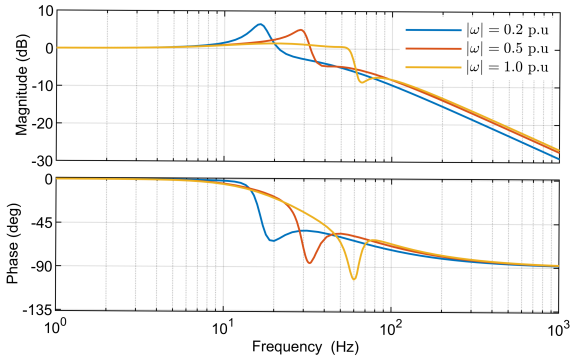


Fig. 5. Frequency response plot of the position estimation loop (22); the parameters are $g = 2\pi\cdot 10$ rad/s and $\Omega_\theta = 2\pi\cdot 25$ rad/s at rated torque.

$$\begin{aligned}\boldsymbol{h}_{\theta} &= (s\mathbf{I}+\boldsymbol{G}+\omega\mathbf{J})^{-1}(s\mathbf{I}+\omega\mathbf{J})\,\hat{\boldsymbol{\lambda}}^{a}_{\hat{d}q} \\ \boldsymbol{h}_{v} &= -(s\mathbf{I}+\boldsymbol{G}+\omega\mathbf{J})^{-1}\,\hat{\boldsymbol{v}}_{\hat{d}q}\end{aligned} \tag{16b}$$

where $\tilde{\boldsymbol{x}} = \begin{bmatrix}\tilde{\theta} & \tilde{v}_{dc}\end{bmatrix}^{\mathrm{T}}$. The transfer function matrices $\boldsymbol{h}_\theta$ and $\boldsymbol{h}_v$ are of length $2\times 1$.

### B. Position Estimation Immune to DC-link Voltage

Let $\boldsymbol{\phi}_\theta$ be the position error projection vector ($2\times 1$) and $\epsilon_\theta$ the position error signal ($1\times 1$). The position error projection vector $\boldsymbol{\phi}_\theta$ is designed to be immune from the DC-link voltage error in steady-state; this is formulated using (16) as

$$\boldsymbol{\phi}_\theta^{\mathrm{T}}\,\boldsymbol{h}_v\,\big|_{s=0} = 0 \quad\Longrightarrow\quad \boldsymbol{\phi}_\theta^{\mathrm{T}}\,(\boldsymbol{G}+\omega\mathbf{J})^{-1}\,\hat{\boldsymbol{v}}_{\hat{d}q} = 0. \tag{17}$$

Also, a unitary open-loop dc-gain (steady-state) of the position estimation loop is desired, i.e.,

$$\boldsymbol{\phi}_\theta^{\mathrm{T}}\,\boldsymbol{h}_\theta\,\big|_{s=0} = 1 \quad\Longrightarrow\quad \boldsymbol{\phi}_\theta^{\mathrm{T}}\,(\boldsymbol{G}+\omega\mathbf{J})^{-1}\,\omega\mathbf{J}\,\hat{\boldsymbol{\lambda}}^{a}_{\hat{d}q} = 1. \tag{18}$$

The preceding two conditions are satisfied with a projection vector of nature:

$$\boldsymbol{\phi}_\theta^{\mathrm{T}} = \frac{-1}{\omega\,\boldsymbol{v}^{\mathrm{T}}_{\hat{d}q}\,\hat{\boldsymbol{\lambda}}^{a}_{\hat{d}q}}\;\hat{\boldsymbol{v}}^{\mathrm{T}}_{\hat{d}q}\,\mathbf{J}\,(\boldsymbol{G}+\omega\mathbf{J}). \tag{19}$$

### C. Speed and Position Observer

A conventional phase-locked-loop (PLL) with a proportional-integral (PI) controller is employed to drive the position error signal $\epsilon_\theta$ to zero as

$$\hat{\omega} = k_p\,\epsilon_\theta + \omega_i \qquad \omega_i = \int k_i\,\epsilon_\theta\,\mathrm{d}t \qquad \hat{\theta} = \int \hat{\omega}\,\mathrm{d}t \tag{20}$$

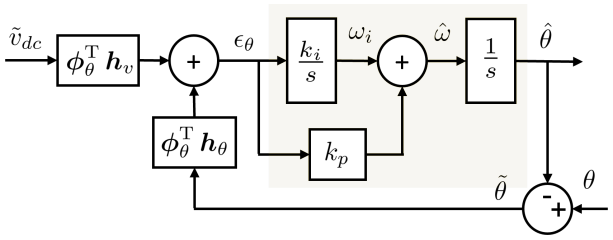


Fig. 6. Analysis of the impact of the DC-link voltage error on the rotor position estimation.

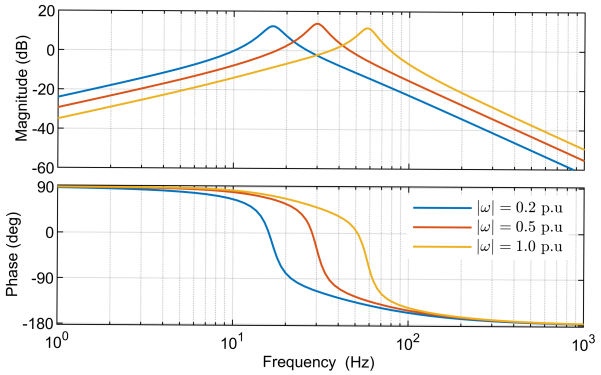


Fig. 7. Frequency response plot of the transfer function between estimated position and the DC-link voltage error (23); the parameters are $g = 2\pi \cdot 10$ rad/s and $\Omega_\theta = 2\pi \cdot 25$ rad/s at rated torque.

where $k_p$ and $k_i$ are the respective gains. The gains of the PLL are tuned for a critically damped response considering $\epsilon_\theta = \tilde{\theta}$ at $s = -\Omega_\omega$ as

$$k_p = 2\,\Omega_\omega \qquad k_i = \Omega_\omega^2 \tag{21}$$

The closed loop transfer function of the position estimation loop, shown in Fig. 4, is given by

$$\frac{\hat{\theta}}{\theta} = \frac{\boldsymbol{\phi}_\theta^{\mathrm{T}}\,\boldsymbol{h}_\theta\,(k_p\,s + k_i)}{s^2 + \boldsymbol{\phi}_\theta^{\mathrm{T}}\,\boldsymbol{h}_\theta (k_p\,s + k_i)}. \tag{22}$$

The frequency response plot of the transfer function (22) is shown in Fig. 5 at rated torque for different speeds; the response depends on the operating point because the projection vector is designed for steady-state conditions in (17) and (18).

Using (19) and (16), the transfer function between the DC-link voltage error and position error, shown in Fig. 6, can be derived as

$$\frac{\hat{\theta}}{\tilde{v}_{dc}} = \frac{\boldsymbol{\phi}_\theta^{\mathrm{T}}\,\boldsymbol{h}_v\,(k_p\,s + k_i)}{s^2 + \boldsymbol{\phi}_\theta^{\mathrm{T}}\,\boldsymbol{h}_\theta\,(k_p\,s + k_i)}. \tag{23}$$

The frequency response plot of the transfer function (23) is shown in Fig. 7 where the immunity of the position observer to the steady-state DC-link voltage error is evidenced.

### *D. DC-link Voltage Adaptation Law*

In addition to the position estimation, an additional and supplementary adaptation loop for the DC-link voltage estimation can be designed. Let $\boldsymbol{\phi}_v$ be the DC-link voltage error projection vector and $\epsilon_v$ the voltage error signal as

$$\epsilon_v = \boldsymbol{\phi}_v^{\mathrm{T}}\,(\hat{\boldsymbol{\lambda}}_{\hat{d}q} - \boldsymbol{\lambda}^i_{\hat{d}q}). \tag{24}$$

To decoupled DC-link voltage estimation and the position estimation loops, the orthogonal projection vector to the position error projection vector is considered, i.e.,

$$\boldsymbol{\phi}_v^{\mathrm{T}}\,\boldsymbol{\phi}_\theta = 0. \tag{25}$$

Also, a unitary open-loop dc-gain of the DC-link voltage estimation loop is desired, i.e.,

$$\boldsymbol{\phi}_v^{\mathrm{T}}\,\boldsymbol{h}_{\tilde{v}}\,\big|_{s=0} = 1. \tag{26}$$

From the preceding two conditions, the DC-link voltage projection vector of nature is given by

$$\boldsymbol{\phi}_v^{\mathrm{T}} = -\frac{\omega\,\hat{\boldsymbol{v}}_{\hat{d}q}^{\mathrm{T}}\,\hat{\boldsymbol{\lambda}}^a_{\hat{d}q}}{|\hat{\boldsymbol{v}}_{\hat{d}q}|^2}\,\boldsymbol{\phi}_\theta^{\mathrm{T}}\,\mathbf{J} \tag{27}$$

Finally, the DC-link voltage adaptation law is defined as

$$\hat{v}_{dc} = v_{dc,n} + v_{dc,n} \cdot \int k_v\,\epsilon_v\,\mathrm{d}t \tag{28}$$

where $k_v$ is the integral gain. The closed loop transfer function of the DC-link voltage estimation, shown in Fig. 8, can be expressed as

$$\frac{\hat{v}_{dc}}{v_{dc}} = \frac{\boldsymbol{\phi}_v^{\mathrm{T}}\,\boldsymbol{h}_v\,k_v}{s + \boldsymbol{\phi}_v^{\mathrm{T}}\,\boldsymbol{h}_v\,k_v}. \tag{29}$$

The frequency response plot of the DC-link voltage estimation loop (29) is shown in Fig. 9 for different speeds at rated torque. A low bandwidth $k_v = 2\pi \cdot 3$ rad/s is chosen for the slow dynamics of the DC-link voltage.

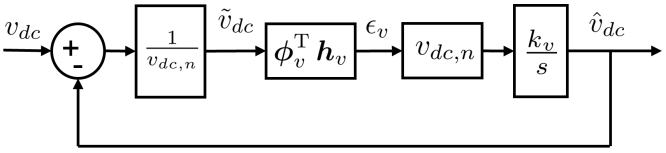


Fig. 8. Block diagram of the closed loop transfer function of the loop DC-link voltage estimation loop (29).

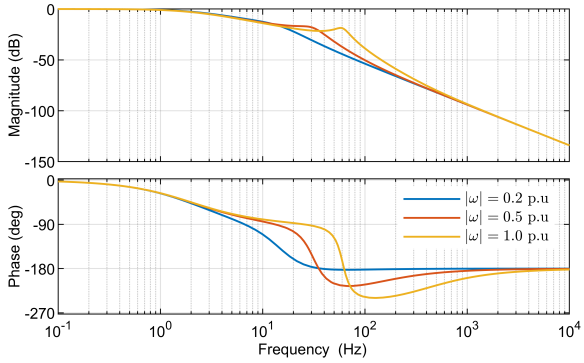


Fig. 9. Frequency response plot of the DC-link voltage estimation loop transfer function (29); the parameters are $g = 2\pi \cdot 10$ rad/s and $k_v = 2\pi \cdot 3$ rad/s at rated torque.

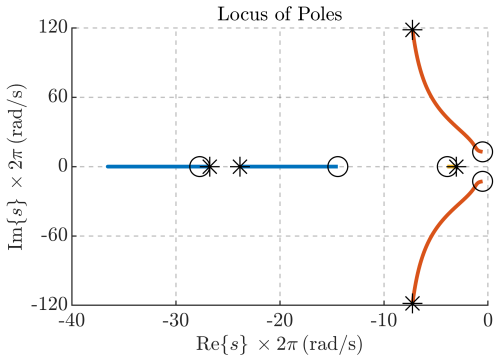


Fig. 10. Locus of poles of the state space model (32) at rated torque where the markers ∘ and ∗ denotes the angular speeds $\omega = 0.1$ p.u. and $\omega = 2$ p.u., respectively. Color code: the stator flux observer poles are in red, the DC-link voltage adaptation pole is in yellow and the position observer poles are in blue. The parameters are $g = 2\pi \cdot 10$ rad/s, $\Omega_\theta = 2\pi \cdot 25$ rad/s and $k_v = 2\pi \cdot 3$ rad/s.

### E. Stability Analysis

The state space model of the proposed scheme is developed to assess the system stability comprising of the stator flux observer, the position observer and the DC-link voltage adaptation. To this end, the error dynamics of the position observer in (20) can be expressed as

$$s\,\tilde{\theta} = \tilde{\omega}_i - k_p\,\epsilon_\theta \qquad s\,\tilde{\omega}_i = -k_i\,\epsilon_\theta. \tag{30}$$

The error dynamics of the relative DC-link voltage error (28) can be expressed as

$$s\,\tilde{v}_{dc} = -k_v\,\epsilon_v. \tag{31}$$

Finally, the combined dynamics of the system is given by

$$s\,\boldsymbol{y} = \boldsymbol{A}\,\boldsymbol{y} \tag{32}$$

$$\boldsymbol{A} = \begin{bmatrix} -(\boldsymbol{G} + \omega\,\mathbf{J}) & \boldsymbol{G}\,\boldsymbol{\lambda}^a_{\hat{dq}} & \mathbf{0} & \hat{\boldsymbol{v}}_{\hat{dq}} \\ k_p\,\boldsymbol{\phi}^{\mathrm{T}}_\theta & -k_p\,\boldsymbol{\phi}^{\mathrm{T}}_\theta\,\boldsymbol{\lambda}^a_{\hat{dq}} & 1 & 0 \\ k_i\,\boldsymbol{\phi}^{\mathrm{T}}_\theta & -k_i\,\boldsymbol{\phi}^{\mathrm{T}}_\theta\,\boldsymbol{\lambda}^a_{\hat{dq}} & 0 & 0 \\ k_v\,\boldsymbol{\phi}^{\mathrm{T}}_v & -k_v\,\boldsymbol{\phi}^{\mathrm{T}}_v\,\boldsymbol{\lambda}^a_{\hat{dq}} & 0 & 0 \end{bmatrix}$$

where $\boldsymbol{y} = \left[\left(\tilde{\boldsymbol{\lambda}}_{\hat{dq}}\right)^{\mathrm{T}} \quad \tilde{\theta} \quad \tilde{\omega}_i \quad \tilde{v}_{dc}\right]^{\mathrm{T}}$. The eigenvalues of (32) are computed for each operating point to evaluate the system stability. The locus of poles of the state space model at rated torque is shown in Fig. 10 where system is observed to be stable at different speeds.

## IV. Simulation

The parameters of the PM-SyR motor are tabuled in Table. I. The $dq$ current references are computed for the maximum-torque-per-ampere (MTPA) condition and realized using the current vector control (CVC). The following simulation considers absence of DC-voltage measurement where the nominal value is used. The flux observer gain is $g = 2\,\pi \cdot 10$ rad/s. The current controller poles are placed at $\Omega_{dq} = 2\pi \cdot 75$ rad/s for critical damping. Likewise, the speed/position observer poles are placed at $\Omega_\omega = 2\pi \cdot 25$ rad/s. The integral gain for the DC-link voltage adaptation is $k_v = 2\pi \cdot 3$ rad/s.

TABLE I
Motor Parameters

| Parameters | Symbol | Values | Units |
|---|---|---|---|
| Rated power | $P_n$ | 5.5 | kW |
| Rated voltage | $V_n$ | 260 | V |
| Rated speed | $\omega_n$ | 1800 | rpm |
| Rated current | $I_n$ | 16.3 | A |
| Rated torque | $T_n$ | 30 | Nm |
| Pole pairs | $p$ | 2 | - |
| Stator resistance | $R_s$ | 0.46 | Ω |
| Shaft inertia | $J$ | 0.02 | $\mathrm{kgm}^2$ |

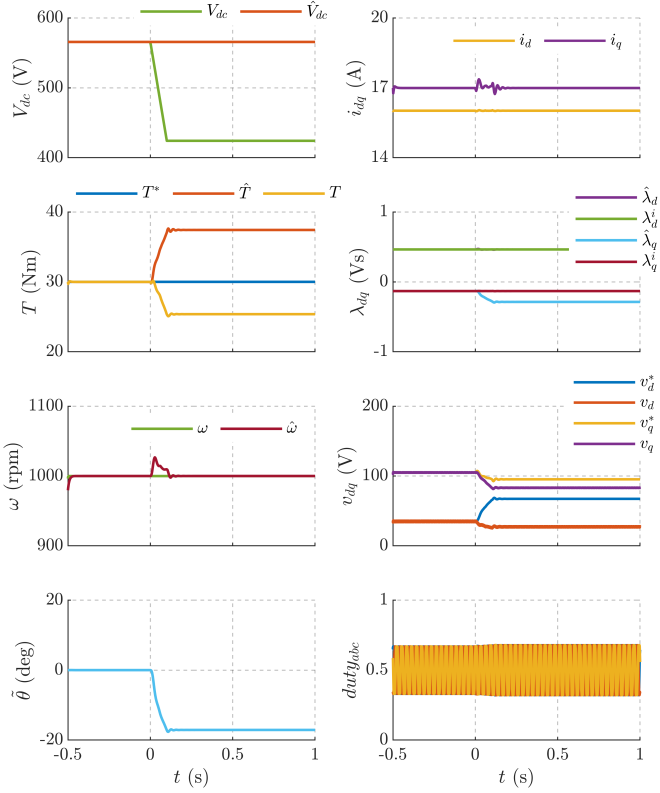


Fig. 11. Simulation validation of the active-flux position observer when the DC-link voltage drops by 25% at $t = 0$.

### A. Active Flux Sensorless Control without Voltage Adaptation

Active flux [5], [13], [14] is among the state-of-art position observers. Fig. 11 shows the result for active flux position observer without the voltage adaptation in torque control mode at 1000 rpm and rated torque. As mentioned earlier, a constant nominal value of DC-link voltage is used without measurement. A reduction in DC-link voltage by 25% occurs at $t = 0$ s. For the time span $t > 0.1$ s, a steady-state position error $\tilde{\theta} = -17°$ is observed due to the DC-link voltage error. The commanded torque reference is $T^* = 30$ Nm while the real torque is $T = 25$ Nm, resulting in a 17% torque error. Moreover, the estimated torque and stator flux are inaccurate due to the discrepancy between the reference and the real voltage. This shows that the active flux method is

susceptible to the DC-link measurement fluctuations and could be potentially unstable.

### *B. Proposed Position Observer With Voltage Adaptation*

The validation of the proposed sensorless scheme is shown in Fig. 12 for the same operating conditions as the preceding test. The voltage adaption is disabled for the time $t < 0.5$ s. Unlike the result in Fig. 11, the proposed scheme in Fig. 12 has negligible steady-state position error in the time $t > 0$ s when the DC-link voltage drops by 25%; also, note that the torque error is zero, i.e., $T^* = T$. When the DC-link voltage adaptation is enabled at $t = 0.5$ s, the stator flux and torque estimation converges to its correct value. This is a supplementary feature exploiting the two degrees of freedom that finds significance in advanced drive applications where accurate stator flux/torque estimation is necessary.

## V. Conclusion

This paper proposed a novel sensorless control technique that is designed to be immune to the errors in the DC-link voltage. This is realized in the projection vector framework based on the linearized flux observer error dynamics. For additional reliability, a supplementary DC-link voltage adaptation is developed that is independent and decoupled from the position estimation. This allows for the case of both position sensorless and DC-link voltage sensorless operation capability. The stability of the proposed sensorless technique along with the voltage adaptation has been evaluated analytically. The proposed scheme was validated through simulation on a 5.5 kW PM-SyR motor and bench-marked against the state-of-art active flux position observer where the voltage error immunity and the accurate torque tracking properties were demonstrated.

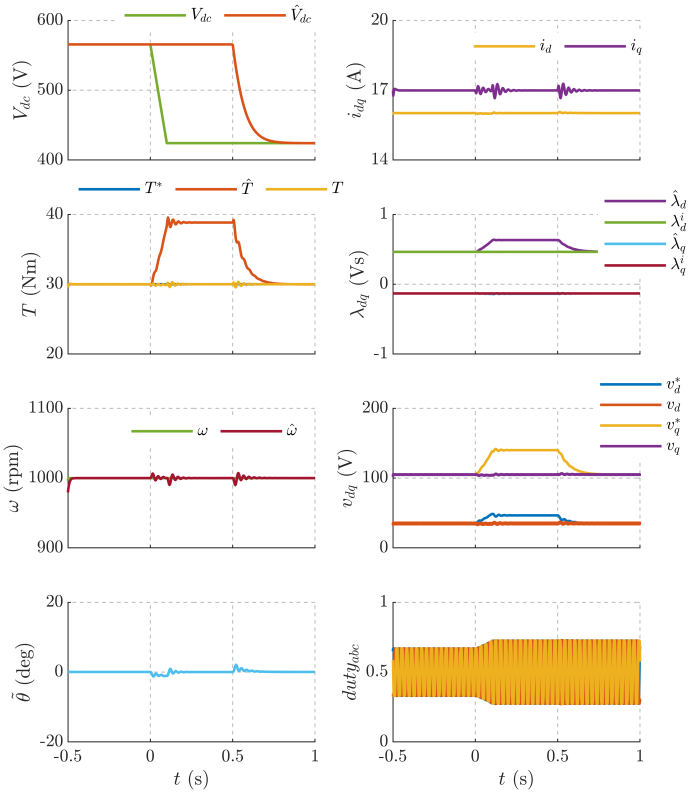


Fig. 12. Simulation validation of the proposed sensorless position observer with voltage adaptation enabled at $t = 0.5$ s.

## References


[1] J. Klima, "Analytical investigation of influence of dc-link voltage ripple on pwm vsi fed induction motor drive," in *2006 1ST IEEE Conference on Industrial Electronics and Applications*, 2006, pp. 1–7.

[2] H. Ouyang, K. Zhang, P. Zhang, Y. Kang, and J. Xiong, "Repetitive compensation of fluctuating dc link voltage for railway traction drives," *IEEE Transactions on Power Electronics*, vol. 26, no. 8, pp. 2160–2171, 2011.

[3] A. Varatharajan, G. Pellegrino, and E. Armando, "Signal-injection sensorless control of synchronous reluctance machines for overload operation," *IEEE Transactions on Power Electronics*, vol. 37, pp. 5874–5883, 2022.

[4] V. Manzolini and S. Bolognani, "On the rotor position self-sensing capability of reluctance and ipm synchronous motors," *IEEE Transactions on Industry Applications*, vol. 56, pp. 3755–3766, 2020.

[5] M. Hinkkanen, S. E. Saarakkala, H. A. A. Awan, E. Mölsä, and T. Tuovinen, "Observers for sensorless synchronous motor drives: Framework for design and analysis," *IEEE Transactions on Industry Applications*, vol. 54, pp. 6090–6100, 2018.

[6] Y. Lee and S. K. Sul, "Model-based sensorless control of an ipmsm with enhanced robustness against load disturbances based on position and speed estimator using a speed error," *IEEE Transactions on Industry Applications*, vol. 54, pp. 1448–1459, 2018.

[7] Y. seok Jeong, S.-K. Sul, S. E. Schulz, and N. R. Patel, "Fault detection and fault-tolerant control of interior permanent-magnet motor drive system for electric vehicle," *IEEE Transactions on Industry Applications*, vol. 41, pp. 46–51, 1 2005.

[8] F. R. Salmasi, T. A. Najafabadi, and P. J. Maralani, "An adaptive flux observer with online estimation of dc-link voltage and rotor resistance for vsi-based induction motors," *IEEE Transactions on Power Electronics*, vol. 25, pp. 1310–1319, 5 2010.

[9] Q. Teng, J. Tian, J. Duan, H. Cui, J. Zhu, and Y. Guo, "Sliding-mode mra observer-based model predictive current control for pmsm drive system with dc-link voltage sensorless," 2017, pp. 1–6.

[10] S. K. Kommuri, S. B. Lee, Y. Park, and K. C. Veluvolu, "A robust voltage, speed and current sensors fault-tolerant control in pmsm drives," 2017, pp. 2937–2942.

[11] E. Armando, R. I. Bojoi, P. Guglielmi, G. Pellegrino, and M. Pastorelli, "Experimental identification of the magnetic model of synchronous machines," *IEEE Transactions on Industry Applications*, vol. 49, pp. 2116–2125, 2013.

[12] A. Varatharajan and G. Pellegrino, "Sensorless synchronous reluctance motor drives: A general adaptive projection vector approach for position estimation," *IEEE Transactions on Industry Applications*, vol. 56, pp. 1495–1504, 2020.

[13] S. C. Agarlita, I. Boldea, and F. Blaabjerg, "High-frequency-injection-assisted 'active-flux'-based sensorless vector control of reluctance synchronous motors, with experiments from zero speed," *IEEE Transactions on Industry Applications*, vol. 48, pp. 1931–1939, 2012.

[14] A. Yousefi-Talouki, P. Pescetto, G. Pellegrino, and I. Boldea, "Combined active flux and high-frequency injection methods for sensorless direct-flux vector control of synchronous reluctance machines," *IEEE Transactions on Power Electronics*, vol. 33, pp. 2447–2457, 2018.